H2020 STRATOFLY Project: from Europe to Australia in less than 3 hours

ICAS 2021 SHANG HAI
International Council of the Aeronautical Sciences
32nd Congress of the International Council of the Aeronautical Sciences
September 6-10, 2021
Pudong Shangri-La, Shanghai, China

H2020 STRATOFLY PROJECT: FROM EUROPE TO AUSTRALIA IN LESS THAN 3 HOURS

N. Viola[1*], R. Fusaro[1], Davide Ferretto[1], Oscar Gori[1], Bayindir Saracoglu[2], Ali Can Ispir[2], Christophe Schram[2], Volker Grewe[3], Johannes Friedrich Plezer[3], Jan Martinez[4], Marco Marini[5], L. Cutrone[5], G. Saccone[5], Santiago Hernandez[6], Karel Lammers[7], Axel Vincent[8], Didier Hauglustaine[9], Bernd Liebhardt[10], Florian Linke[10], Daniel Bodmer[10], Thommie Nilsson[11], Christer Fureby[11], Christian Ibron[12]

[1]Mechanical and Aerospace Engineering Department, Politecnico di Torino, Corso Duca degli Abruzzi 24, 10129 Turin, Italy

[2]Von Karman Institute for Fluid Dynamics, Waterloosesteenweg 72, B-1640 Sint-Genesius-Rode, Belgium.

[3] Institut für Physik der Atmosphäre, Deutsches Zentrum für Luft- und Raumfahrt (DLR) Oberpfaffenhofen, Münchner Straße 20, 82234 Wessling, Germany

[4] Institute of Aerodynamics and Flow Technology, Deutsches Zentrum für Luft- und Raumfahrt (DLR) Oberpfaffenhofen, Münchner Straße 20, 82234 Wessling, Germany

[5] Centro Italiano Ricerche Aerospaziali, Via Maiorise - 81043 Capua (CE), Italy

[6] Department of Construction Technology, University of La Coruna, Rúa da Maestranza 9, 15001 A Coruña, Spain

[7]Netherlands Aerospace Centre, Anthony Fokkerweg 2, 1059 CM Amsterdam, The Netherlands

[8]Department of Multi-Physic for Energetics, The French Aerospace Lab ONERA, FR-91123 PALAISEAU, France

[9]Laboratoire des Sciences du Climat et de l'Environnement (LSCE), CNRS, Gif-sur-Yvette CEDEX – France

[10]Technical University of Hamburg Harburg, Am Schwarzenberg-Campus, 21073 Hamburg, Germany

[11] Lund University, Department of Energy Sciences / Heat Transfer, P.O. Box 118, SE-221 00 Lund, Sweden

[12] Swedish Defence Research Agency, FOI Totalförsvarets forskningsinstitut 164 90 Stockholm (Sweden)

nicole.viola@polito.it

Abstract

As eluded in previous studies, with special reference to those carried out in the European framework, some innovative high-speed aircraft configurations have now the potential to assure an economically viable high-speed aircraft fleet. They make use of unexploited flight routes in the stratosphere, offering a solution to the presently congested flight paths while ensuring a minimum environmental impact in terms of emitted noise and green-house gases, particularly during stratospheric cruise. However, only a dedicated multi-disciplinary integrated design approach could realize this, by considering airframe architectures embedding the propulsion systems as well as meticulously integrating crucial subsystems. In this context, starting from an in-depth investigation of the current status of the activities, the STRATOFLY project has been funded by the European Commission, under the framework of Horizon 2020 plan, with the aim of assessing the potential of this type of high-speed transport vehicle to reach Technology Readiness Level (TRL) 6 by 2035, with respect to key technological, societal and economical aspects. This paper aims at summarizing the main results achieved so far to solve the main issues related to thermal and structural integrity, low-emissions combined propulsion cycles, subsystems design and integration, including smart energy management, environmental aspects impacting climate change, noise emissions and social acceptance, and economic viability accounting for safety and human factors.

Keywords: High-speed transportation, Technological Challenges, Environmental Sustainability

1. Introduction

The worldwide incentive to reconsider commercial high-speed transport urges Europe to quantitatively assess the potential of civil high-speed aviation with respect to technical, environmental and economic viability in combination with human factors, social acceptance, implementation and operational aspects. High-speed commercial flights could be significantly beneficial for long-haul routes to virtually shrink the globe and shorten the time of flight of one order of magnitude for antipodal destinations, thus revolutionizing the present idea of business trips and touristic travels. The satisfaction of this need can however be seriously hampered by the compliance with the environmental sustainability requirements that currently represent the main goal for aviation, unless innovative technological solutions are investigated, developed and eventually integrated and validated in operative aircraft. The higher is the speed of flight, the higher is the fuel consumption and consequently emissions, unless breakthrough technologies can intervene to break down this obvious conclusion. In order to allow for low environmental impact and de-carbonization of air travels by 2050, new solutions need to be designed for the various ranges of flight routes, thus leading to different aircraft configurations and enabling technologies for short, medium and long-haul range missions.

As far as long-haul flights are concerned, the targets of zero CO2 emissions and shorter times of flight urge to seek new solutions in terms of propellant, aircraft configuration and technologies. To shorten the time of flight and to fulfil the requirement of long-haul routes, high speed air-breathing propulsion shall be considered, innovative aircraft configuration with high aerodynamic efficiency shall be targeted [1] and liquid hydrogen, that guarantees complete de-carbonization, shall be exploited as not drop-in fuel, thanks to its high specific energy content. Shorter time of flights and long-haul routes are the two crucial mission requirements that have led to a new concept of aircraft for high-speed long-haul routes that has been named STRATOFLY MR3. STRATOFLY MR3 is the reference vehicle of the H2020 STRATOFLY project, a highly-multidisciplinary project, funded by European Commission within the framework of the Horizon 2020 Program. STRATOFLY is the natural follow-on of a series of European Projects (i.e. ATLLAS I/II [2], LAPCAT I/II [3], HIKARI [4], HEXAFLY [5], HEXAFLY Int. [6]) devoted to study the feasibility of the high-speed civil transportation at stratospheric altitudes, with the goal to reduce the duration of antipodal flights of one order of magnitude with respect to current air transport.

The H2020 STRATOFLY project refines the design and the concept of operations of STRATOFLY MR3 vehicle throughout all its flight regimes, including the crucial subsonic and transonic regimes, reaching the ambitious goal of Technology Readiness Level (TRL) equal 6 by 2035 for the concept, developing crucial technologies which may represent a step forward for future reusable space transportation systems.

After this short introduction, Section 2 briefly presents STRATOFLY MR3 vehicle and mission concepts, while Section 3 discusses the main results achieved so far with respect to the main technical challenges. Eventually main conclusions are drawn together with ideas for future activities.

2. H2020 STRATOFLY: mission concept and reference aircraft

STRATOFLY MR3 vehicle configuration is the result of research activities aimed at refining the promising MR2.4 waverider configuration. Benefitting from the heritage of past European funded projects and, in particular, from the LAPCAT II project, the waverider configuration has been adopted, improved and characterized throughout all flight phases. STARTOFLY MR3 is a highly integrated system, where propulsion, aerothermodynamics, structures and on-board subsystems are strictly interrelated to one another, as highlighted in Fig. 1 [7][8][9].

From the configuration standpoint, the MR3 design clearly appears as driven by its peculiar mission concept, which can be summarized as follows: STRATOFLY MR3 will be able to fly along long-haul routes reaching Mach 8 during the cruise phase at a stratospheric altitude ($h > 30{,}000$ m) carrying 300 passengers as payload. Fig. 1 shows STRATOFLY MR3 external configuration. STRATOFLY MR3 has a waverider configuration with the engines and related air duct embedded into the airframe and located at the top. The integration of the propulsive system at the top of the vehicle allows maximizing the available planform for lift generation without additional drag penalties, thus increasing the aerodynamic efficiency, and it allows optimizing the internal volume. This layout guarantees

furthermore to expand the jet to a large exit nozzle area without the need to perturb the external shape which would lead to extra pressure drag.

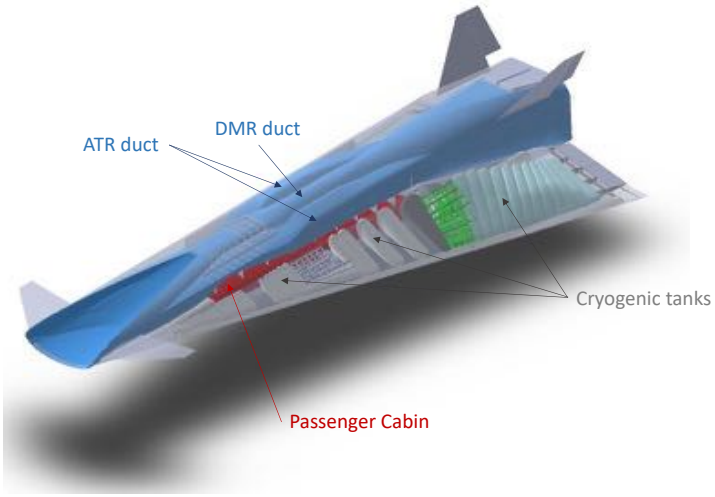

Fig. 1. STRATOFLY MR3 vehicle layout and subsystems integration

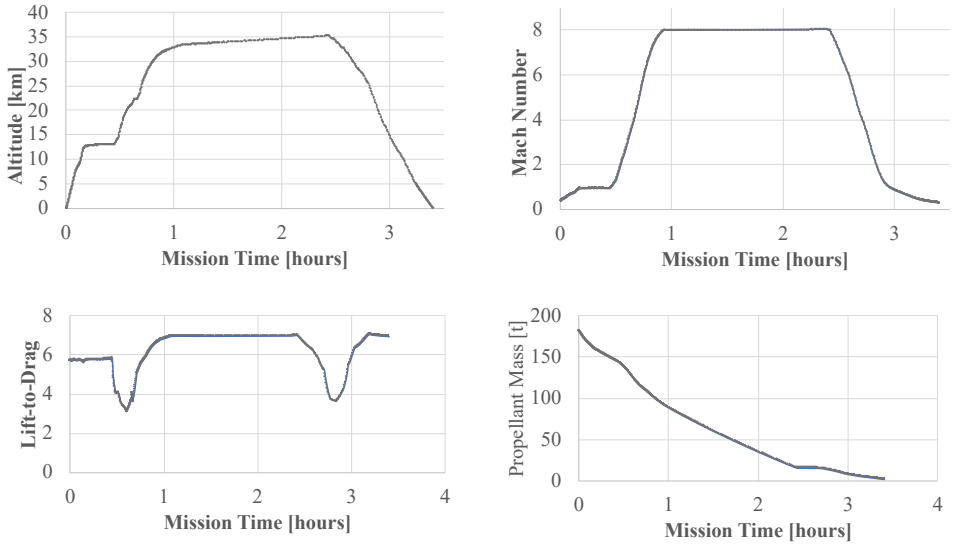

Fig. 2. STRATOFLY MR3 BRU-SYD Reference Mission

The reference mission profile (Fig. 2), initially based on the published MR2.4 reference trajectory [10], has been improved thanks to (i) the introduction of more detailed and reliable aerodynamic and propulsive databases [11], (ii) the optimization of the depletion strategy to minimize the variation of the centre of gravity position and (iii) the redesign of the Flight Control System. During the first part of the mission the ATR engines are used and the vehicle performs the first climb phase, which terminates at Mach = 0.95 and at an altitude between 11 and 13 km. The air turbo–rocket (ATR) is a particular case of turbine-based combined cycles cycle engines which brings together elements of the turbojet and rocket motors and provides a unique set of performance characteristics. This engine offers a high thrust-to-weight ratio and specific thrust over a wide range of speed and altitude, constituting an excellent choice as an accelerator engine up to high-supersonic speeds. Then, the vehicle performs the subsonic cruise. This phase is needed to prevent a sonic boom while flying over land. A constraint on the distance flown from the departure site should be considered to fulfil this requirement: the subsonic cruise phase ends when the vehicle is at 400 km from the departure airport. Then, the supersonic climb starts, and the vehicle accelerates up to Mach = 4. At the end of this phase, the ATR engines are turned off and the DMR is activated to accelerate up to Mach = 8. Dual Mode Ramjet engine (DMR) is the high-speed engine that can be operated in both ramjet and scramjet modes. The

next phase is the hypersonic cruise: in case of a Europe to Asia or Australia mission, the vehicle points towards the Bering strait, then it flies over the Pacific Ocean to reach the destination. The cruise altitude is in the range between 30 and 35 km. Eventually, the engines are turned off and the vehicle performs the descent towards the landing site.

3. STRATOFLY MR3: CHALLENGES AND GOALS

3.1 Multi-bubble multi-functional structures and materials

The aircraft architecture features a waverider configuration, internally supported by multi-bubble integral cryogenic tanks hosting the LH2 propellant, being one of the major challenges the integration of lightweight structures with the high-speed propulsion system. Additionally, the passengers cabin is also designed leveraging the multi-bubble concept. Given the requirements of the hypersonic flow regime, adequate materials are selected for the aircraft: ceramic matrix composites for the exterior skin and engine, aluminum 2195-T8 for the cryogenic tanks and CFRP for the passenger cabin. The full description of the structural scheme is presented in [12].

3.1.1 Structural scheme

Several structural schemes have been developed to strengthen the most critical areas, both from a stress perspective and to avoid the local vibrational modes present in unstiffened zones of the components.

The multi-bubble architecture has some deficiencies generated by the transition between the cusps of each individual lobe. At these locations a discontinuity in the load path generates stress concentrations that disrupt the membrane behavior of the component. In order to palliate this effect, thin walled shell elements, stress relievers, working under tension have been designed to provide two orthogonal load paths that eliminate the stress concentration (Fig. 4).

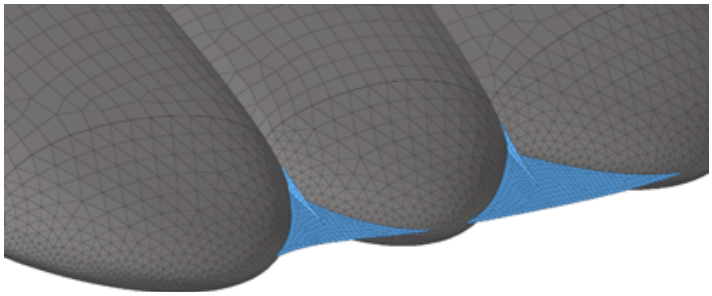

Fig. 3. Stress relievers

Furthermore, in order to fully integrate the main components, lightweight connection elements composed by almost orthogonal grillages have been designed between the cryogenic tanks, skin, passengers cabin and DMR engine. In Fig. 4, the set of ribs in the rear cryogenic tank supporting the engine nozzle are shown.

Due to their size and shape, these tanks, and consequently the wings, are subjected to deflections that significantly alter the exterior aerodynamic profile and cause stress concentrations at the tanks edges. To overcome this issue, a structural scheme in the interior of the tanks is devised. Conceptually, such scheme creates load paths between the top and bottom faces of the bubble in order to reduce deflections and stresses. To prevent a reduction in the tanks capacity, the new elements have to be located in the webs between bubbles. Taking into account the complex geometry of the tanks, the adequate design of these elements is far from obvious. For that reason, a slew of alternatives is considered, ranging from simple tension rods to a complete wall. To obtain an efficient arrangement, a topology optimization has been performed. The results of the topology optimization have to be subjected to an engineering interpretation to be realized into a comprehensible structure. Judging by the general aspect of the concentration of material density and, more importantly, the fact that, in a static analysis, those elements are exclusively working under tension, it is opted for an array of tension rods as the more suitable solution. The topology optimization for one of the wing tanks is shown in Fig.

5.

Fig. 4. Rear pillow configuration

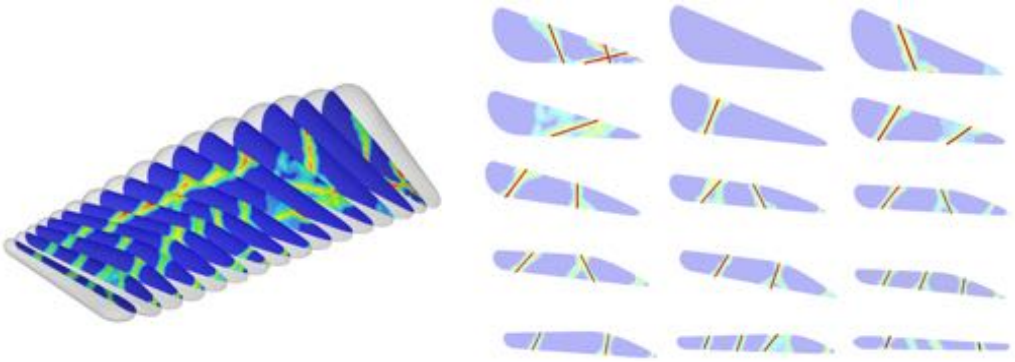

Fig. 5. Topology optimization of the wing tanks

3.1.2 Single and multi-objective optimization

After obtaining a satisfactory vehicle design, the complete sizing of the aircraft has been performed. To do so, a bi-level optimization strategy has been developed [13]. Using this methodology, the full structural configuration including all the stringer dimensions is obtained for the required volumes of the aircraft. The full procedure is summarized in Fig. 6. After appropriately subdividing the component, an optimization from a global perspective is performed. Then, the structural response is used to analyze local models in the second level optimization, where a full description of the structural scheme is achieved. Finally, an anisotropic-unit-thickness panel which has the same stiffness than the obtained design is used in the global level optimization. The process is repeated until convergence is achieved. The result of the optimization process for the passenger cabin provided a relevant decrease of the mass that changed from an amount of 7542 kg to 4601 kg.

Although satisfactory, the single objective bi-level optimization generates very complex designs. For that reason, a multi-objective optimization considering not only the mass vehicle but also manufacturing considerations as objective function has been formulated. The manufacturability has been quantified by the number of different stringer types considered in the design. In the case of the passengers cabin a range of different types of stringers between 1 and 51 was considered. Fig. 7 shows the Pareto front obtained and the results for four cases with 1, 9, 29 and 51 different types of stringers. The result reveals that the ratio of mass decrease is more relevant from 1 to 9 design variables that from 9 to 51. Thus, the slope of the Pareto front is of paramount importance to allow the designers to decide the best trade-off design according to the requirements.

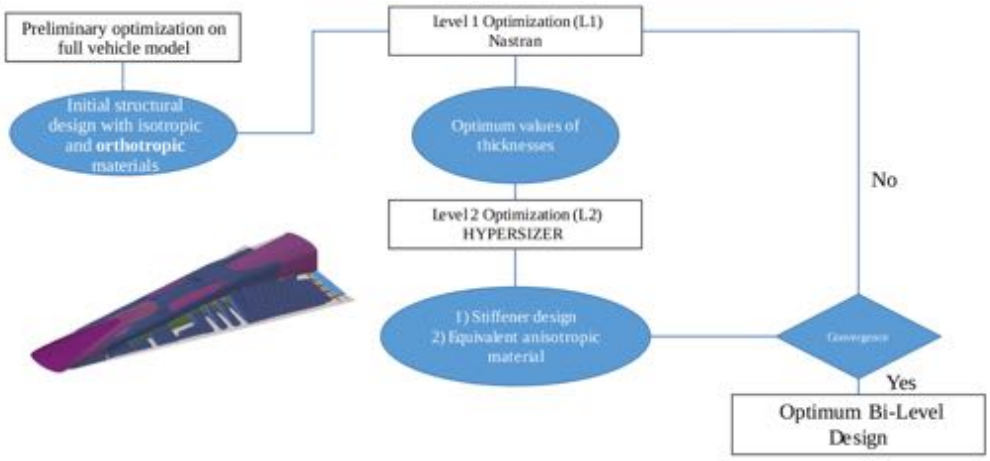

Fig. 6. Flowchart for the bi-level optimization

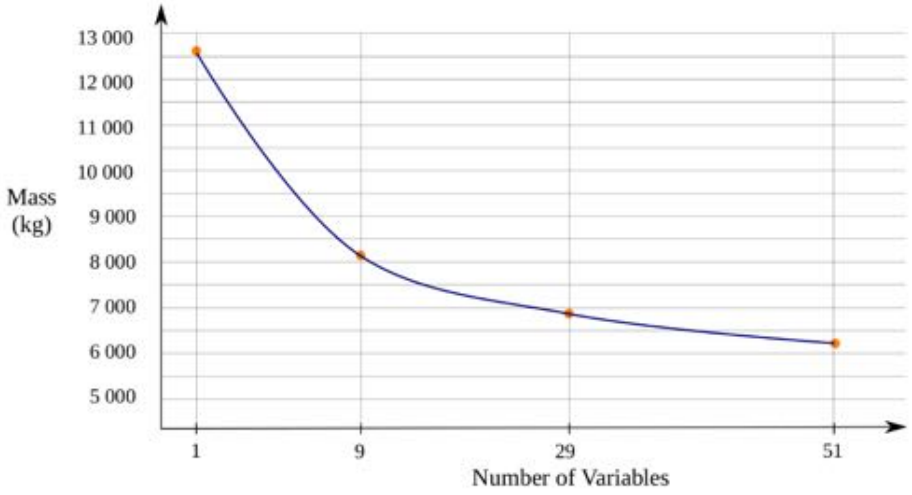

Fig. 7. Pareto front

3.2 Aerodynamics

The aerothermodynamics is one of the main disciplines and the starting point of the design project of the fully integrated STRATOFLY vehicle. It feeds the mission analysis activity as well as the thermal and structural activities.

For the calculation of the thermal loads the challenging cruise condition of Mach 8 has been considered. CFD simulations on a reduced domain at AoA=0 deg for three different rounding (6.25, 11.3 and 22.5 mm) at the intake leading edges have been conducted, the goal being to select the proper rounding by verifying heat fluxes in intake critical areas and intake performance (total pressure recovery, mass flow rate). The cruise conditions at M=8 and 32 km of altitude are characterized by the following far field conditions: P=845.1 Pa, T=222.7 K. Unstructured grids (see Fig. 8-left) were generated by using the ICEMCFD commercial software, constituted of tetrahedral cells inside the bulk volume of the domain and of prisms near the solid surfaces in order to have a better resolution of the local boundary layer. The grid is composed of about 20-million cells.

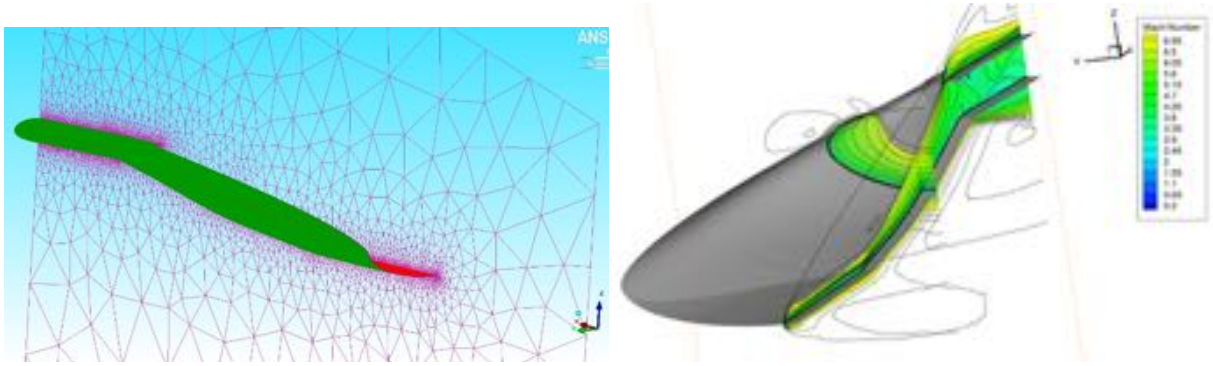

Fig. 8. Grid and Mach 3D contour at M=8

Mach number contours on symmetry plane are shown in Fig. 8-right, where oblique shock waves start from geometry discontinuity and are all captured inside the crotch, while the leading-edge shock goes just a little bit outside. The interaction of local crotch bow-shock and the oblique shock wave happens internally to the combustor inlet, leading to an overload with respect to the leading-edge zone. The maximum of heat flux (hot point) is anyway located near the intake's lateral leading-edge junction and not on the symmetry plane. In this part of the geometry, there is a strong interaction between the above said shocks with the transversal shock wave starting from the lateral leading edge (see Fig. 8-right).
Another important task of the aerodynamic activity consisted in the aerodynamic database development all over the range of Mach number and for all the attitudes and control surfaces deflections, and moreover taking into account both the external and the internal flow path. In order to obtain a complete database a build-up approach based on inviscid CFD simulations and engineering formula for the viscous part has been followed.
In Fig. 9 we can see the inviscid grid of one million of cells for clean (undeflected) configuration and, as an example of aerodynamic database, the drag coefficient versus the Mach number compared with a SIM (Surface Impact Method) code results.

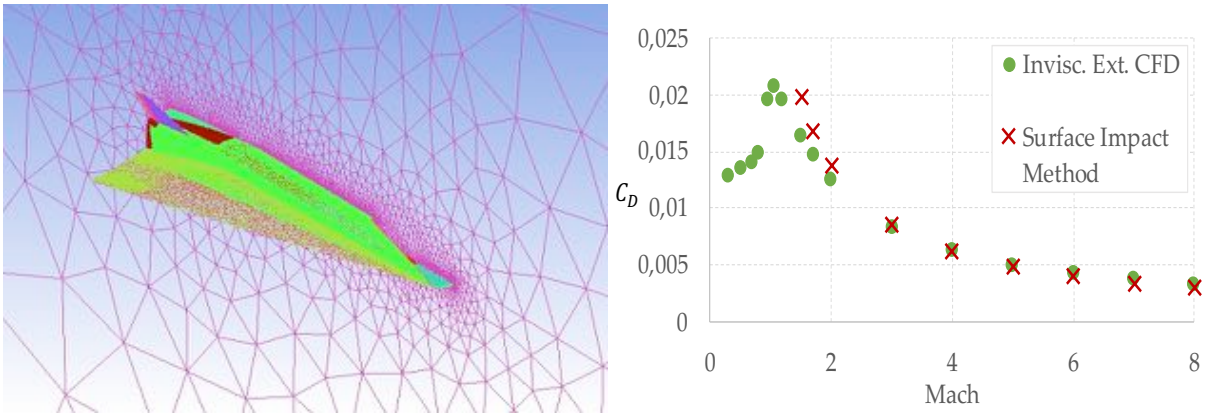

Fig. 9. Inviscid Grid (1M cells) and Drag coefficient vs Mach number

3.3 High-speed propulsion

The High-speed propulsion systems, and in particular the scramjet engines, are the key to extend the airbreathing engine way beyond traditional aircraft limits. Subsonic combustion produces high static pressure and temperature and high heat transfer (heat load) to the engine combustor structure – especially at higher flight Mach number. These static temperature and heat loads place a practical upper limit on subsonic combustion (in ramjet operation) somewhere between Mach 4 and 5. The scramjet overcomes this limit using supersonic combustion. The scramjet has no nozzle throat at the end of the combustor and does not need a turbomachinery compression system, since the required pressure recovery is provided by front oblique shocks: for a hypersonic vehicle, the separation between the engine and the aircraft, typical of conventional subsonic and supersonic configurations, becomes less evident. The SPREAD (Scramjet PREliminary Aerothermodynamic Design) code is a powerful tool to draw a preliminary design of a propulsion system, such as scramjet, ramjet or turbojet, in an

integrated aircraft/engine configuration. The main idea behind SPREAD is that a complex system, such as an airbreathing propulsive system, may be divided into its main components, as compressor, combustor, heat exchanger, nozzle, etc., each of them modelled as a black-box with inputs, outputs and ad-hoc mathematical models to link the outputs to the given inputs.

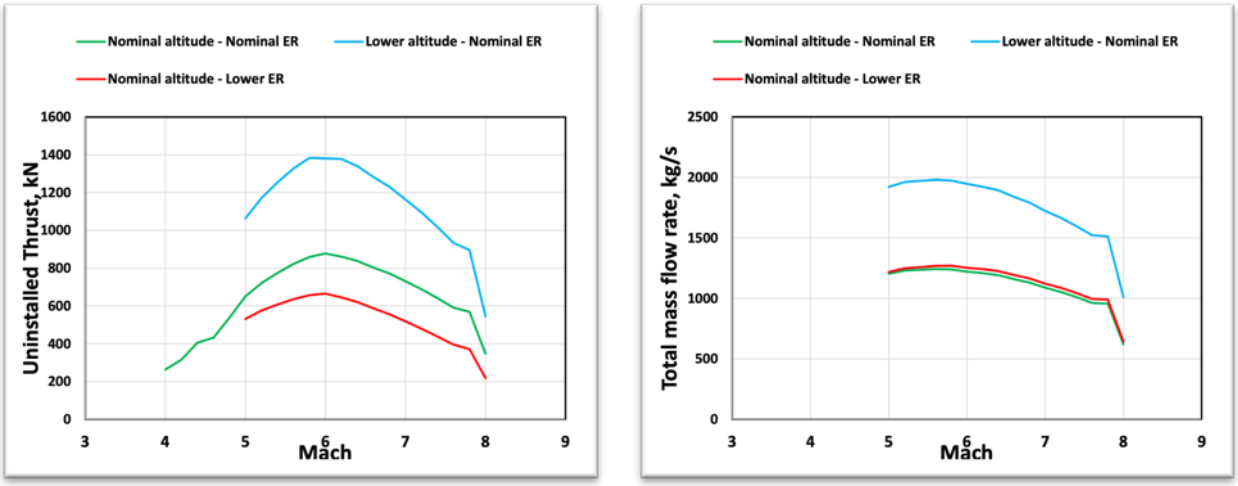

Fig. 10 Uninstalled thrust and total mass flow rate

Fig. 10 shows the computed uninstalled thrusts and the predicted captured mass flow rates, for the a nominal MR3 trajectory with nominal thrust setting (green lines), for a lower altitude (-3km) trajectory (light blue line) and for a lower (-30%) thrust setting (red line). Fig. 11 reports the Emission indexes for NO and H2O, respectively.

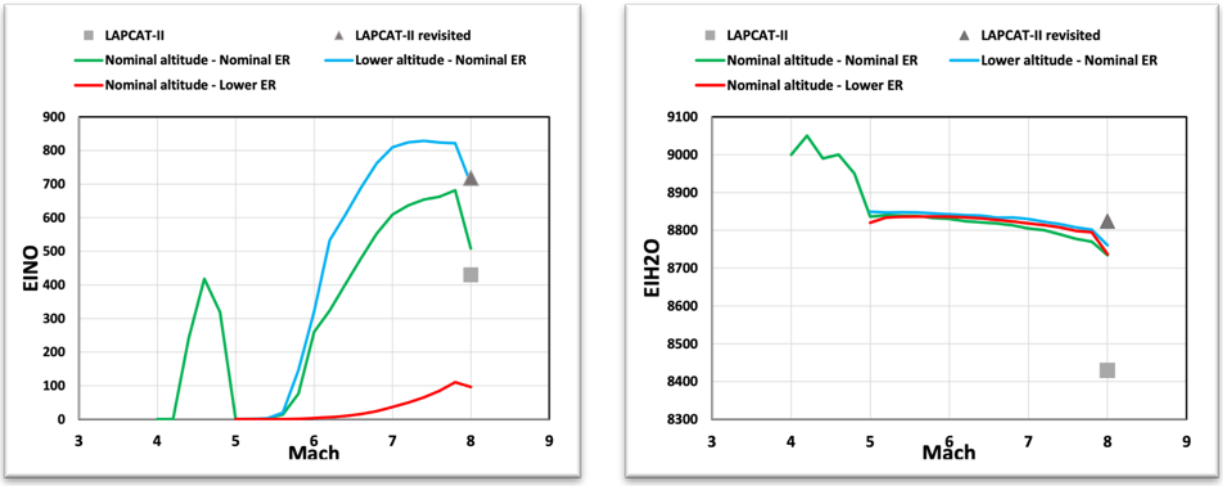

Fig. 11 Emission indexes for NO and H2O

3.4 More efficient and greener propulsion systems

Maximize the potential of embedded high-speed propulsion systems for overall performance by balancing the lift generated by the airframe and the jet contribution through optimization of the advanced propulsion system from thermodynamic cycle level to detailed nose-to-tail simulations of the propulsive duct. To enable jet noise reduction and structural weight reduction, partially or fully embedded engines will be traded-off versus propulsion efficiency. The goal is to reduce the perceived noise emission by 65% without penalizing specific fuel consumption. Finally, having cryogenic fuels on-board provides the opportunity to reach a higher Carnot efficiency and as such to revolutionize engine cycles with a higher thermal efficiency. The cycles allows a 75% to 100% reduction in CO2 emissions per passenger kilometre (ATAG Target) and 90% reduction in NOx emissions. The use of alternative fuels, the optimized design of Dual-Mode Ramjet (DMR) and Dual-Mode Scramjet (DMS)

combustor and injection strategy, and plasma-assisted combustion (PAC) will be part of the emission reduction targets.

The imbedded propulsion system designed for STRATOFLY vehicle enables seamless air-breathing operation from take-off to climb and cruise until descend and landing. The unique propulsion system brings in two distinct engine technologies. For the take-off and supersonic climb phase, the vehicle is propelled by six air-turbo rocket (ATR) engines while the hypersonic phase of the climb and the cruise is powered by a DMR engine. The ATR engines are composed of two stage contra-rotating fans ingesting substantial amount of air which is burned by the Hydrogen fuel and then expanded through a common nozzle shared with DMR engine. The ATR fans are driven by dedicated fuel turbines enclosed with each ATR unit. Two distinct engine technologies are combined on a single propulsion system platform of STRATOFLY MR3 vehicle through an extensive network of regenerative fuel heat exchangers. The heat exchangers are located around the common propulsive nozzle and combustion chamber to recuperate the heat generated by the combustion of Hydrogen to reheat the cryogenic Hydrogen fuel before running the fuel turbine of the ATR and subsequently entering the combustion chambers of ATR and DMR engines. This approaches not only enables the power required for the turbine to run the fans of ATR engines but also increase the overall efficiency of the system.

The operation of the combined cycle propulsion system of STRATOFLY MR3 engine is deeply investigated through 1D models using Ecosimpro software. The thermodynamic performance of each engine component can be simulated by using the ESPSS libraries. The interactions and interdependencies of amongst the components are ensured through ducts and valves which can also be modelled by the software. A special attention was paid to the take-off and supersonic climb phase as they are the most critical section of the low-speed operation of the vehicle where ATR engines provides majority of the thrust.

The performance of the ATR engine was investigated throughout 1D thermodynamic studies, operational envelope was created and cycle optimization was done for several cruise speeds [14]. A propulsive database matrix was also created to investigate the ATR engine behaviour for off-design flight scenarios by changing cruise Mach number, altitude and air-fuel flow mixture ratio. The basic goal of this work is to observe propulsive performance such as thrust, Isp and overall efficiency when the variables in the operational envelope deviate from optimized point. Some propulsive database maps are demonstrated in Fig. 12. Specific impulse, Isp is represented with colourful contours and given in [m/s] unit, the overall efficiency is shown with the lines on the contours.

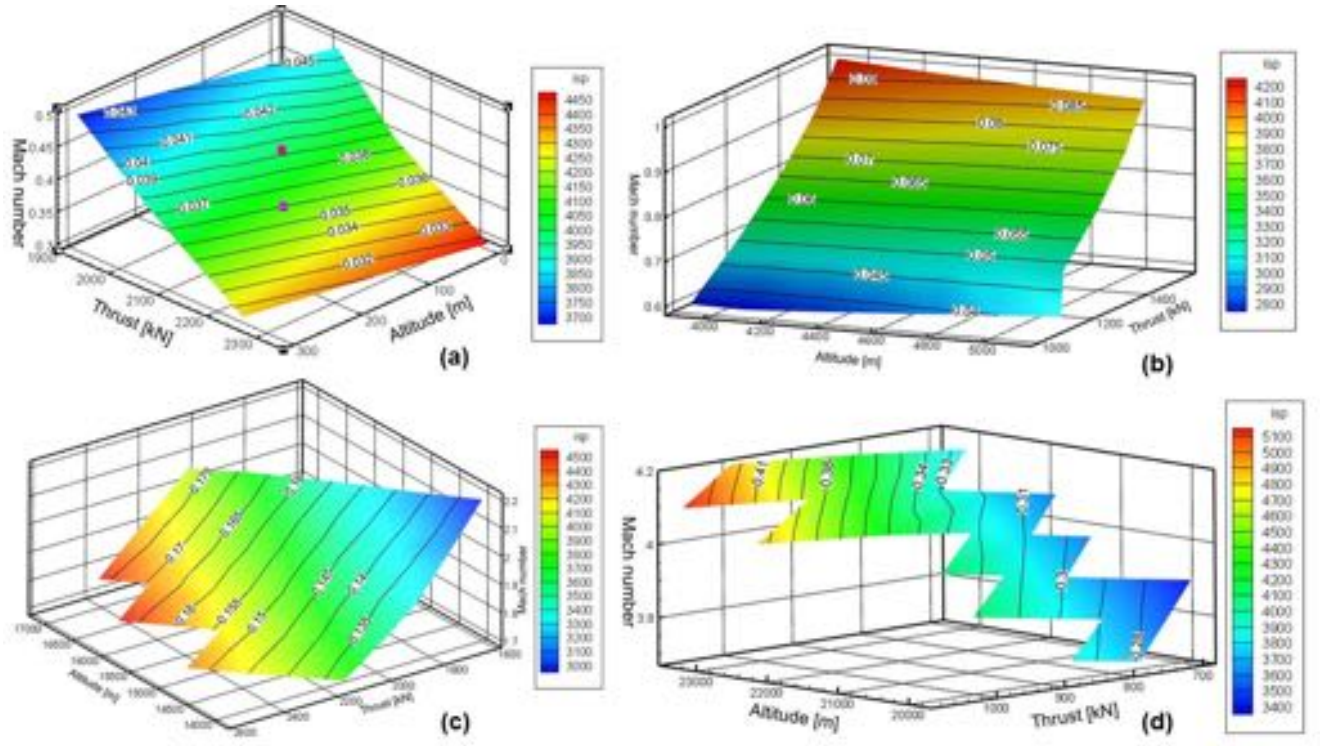

Fig. 12. Propulsive database maps for cruise speeds of Mach 0.3 (a), Mach 0.8 (b), Mach 2 (c), Mach 4 (d)

High fidelity numerical simulations using Finite Rate Chemistry (FRC) Large Eddy Simulations (LES), [15], have been performed to provide additional, supplementary, information regarding the operation of the scramjet engine, and reciprocal validation of the SSFE experiments. The FRC-LES computations are performed using the One Equation Eddy Viscosity (OEEVM) subgrid stress and flux model, [16], together with the Partially Stirred Reactor (PaSR) turbulence-chemistry interaction model, [17]. The chemical reaction mechanism employed is the Z22 hydrogen-air reaction mechanism, [18], supplemented with a 20-step nitrous oxide reaction mechanism. The FRC-LES model has previously been validated, e.g. [19-20] and use the Swedish National Infrastructure for Computing resource Beskow. Fig. 13 shows the computational model of the SSFE. This is a downscaled (1:60) and simplified version of the full-scale STRATOFLY MR 3 flight vehicle, consisting of an inlet, an isolator, a combustor, and an exhaust nozzle. The wings are partially cut to fit the HEG test section, and the combustor is modified to compensate for some of the adverse scaling effects in sub-scale tests. To compensate this, the equivalence ratio of the SSFE was increased to 1.0, and the combustor layout was optimized to reach mixing and combustion efficiencies of ~0.8. Fuel injection is performed on the top of the semi-struts and at the top and bottom of the central strut. A baseline hexahedral grid of ~34 million cells was used: This grid is coarse in the freestream but gradually refined towards the SSFE body, with additional refinement in the engine flow path, and at the SSFE walls, around the semi-struts and the central strut, as well as around the injectors. Dirichlet boundary conditions are used for all variables at the inlet and at the injectors. At the outlet, a Neumann boundary conditions is used, whereas a wall-model is used to model the near-wall flow. The LES Index of Quality, [21], suggest that ~87% of the kinetic energy was resolved, indicating that the grid used is sufficiently fine for an LES computation.

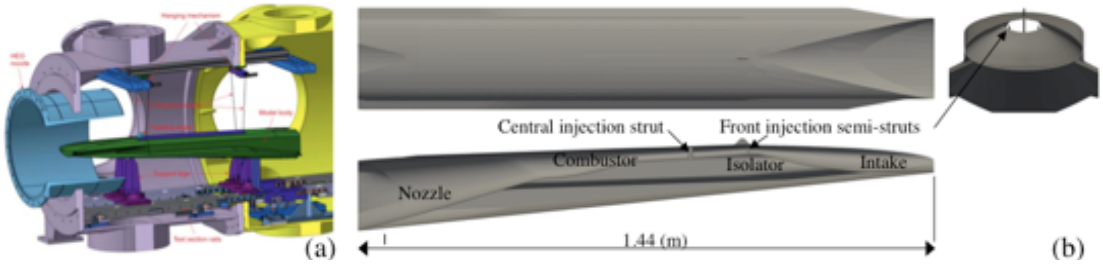

Fig. 13. The SSFE. (a) Schematic of the Small Scale Flight Experiment (SSFE) installed in the HEG test section and (b) CAD views of the computational model of the SSFE flight vehicle

Fig. 14 present side- and top views of the combustor, together with volumetric renderings of the (a) axial velocity, vx, (b) temperature, T, (c), pressure, p, and (d) heat-release, Q, from the FRC-LES. The flow in terms of vx show high velocities along the intake, with the exception of the thin boundary layer developing over the edges and curved surfaces. The flow appears to separate at the lower wall, between and just downstream of the semi-struts. This separation region is shallow and is initiated at the junction between the downstream part of the intake and the upstream part of the combustor. The H2 injected on the top of the semi-struts creates two large vortex structures the dominate the flow throughout the whole combustor. The flow between the semi-struts and the full-strut appears dominated by the large longitudinal vortex structures and the flow and mixing patterns developing as a direct consequence of these, a shock-train developing at the start of the isolator, and the combustor boundary layers. Only limited volumetric expansion is observed in this region since the H2 is about to ignite due to shock impingement. After the full strut, in the 1st combustor section, a decrease in vx observed due to volumetric expansion and increased pressure as a consequence of the H2 being ignited and burning. Further downstream, in the 2nd combustor section, and in the nozzle, vx recovers and increases to provide thrust. The temperature, T, is low all along the intake, except at the walls, but increase at the combustor inlet. Here, T increase due primarily to the intake compression. T is then rather constant until fuel injection and ignition takes place. After ignition, which is mainly due to shock impingement, T increases to around 2600 K at the edges of the H2 jets. When additional H2 is injected sideways from the full-strut ignition occurs throughout the cross-section, and T increases to around 2500 K across the whole cross-section of the 1st combustor section. Further downstream, in the 2nd combustor section, and in the nozzle, the temperature initially prevails but gradually decrease due to the expansion facilitated by the combustor shape. In both the 1st and 2nd combustor sections the

longitudinal vortex structures dominate the large-scale flow, turbulent mixing (at all scales) and the combustion.

The pressure, p, shows very clear imprints of the three-dimensional shock train that develops along the combustor, and particularly downstream of the full-strut, where the effects of the large-scale vortical structures starts to mutually interact with the pressure through baroclinic torque and vortex stretching, influencing mixing at all (resolved) scales. The high-pressure region essentially ends where the 1st combustor section end and the 2nd (weakly diverging) combustor section starts as a consequence of the rapid area increase and flow acceleration. The shock-train is still present along the 2nd (weakly diverging) combustor section, and into the nozzle but rapidly decreases in strength. The pressure influences the rates of the chemical reactions which are significantly enhanced in the 1st and 2nd combustor sections, thus promoting the exothermicity. The heat-release, Q, occurs on the edges of the H2 plumes that are discharged from the semi-struts, after that the H2 at the edge has mixed with the freestream air, and after this mixture have been struck by the shock-train. Some heat-release is also observed just behind the bow-shocks on the top of the semi-struts. The majority of Q is however found to occur just after H2 has been injected sideways from the full-strut ignition. This is due to the high lateral injection speed and large penetration of the H2 as well as the high T resulting from the combustion between the semi-struts and the full-strut, acting as a virtual flame holder for the main flame dominating after the full-strut.

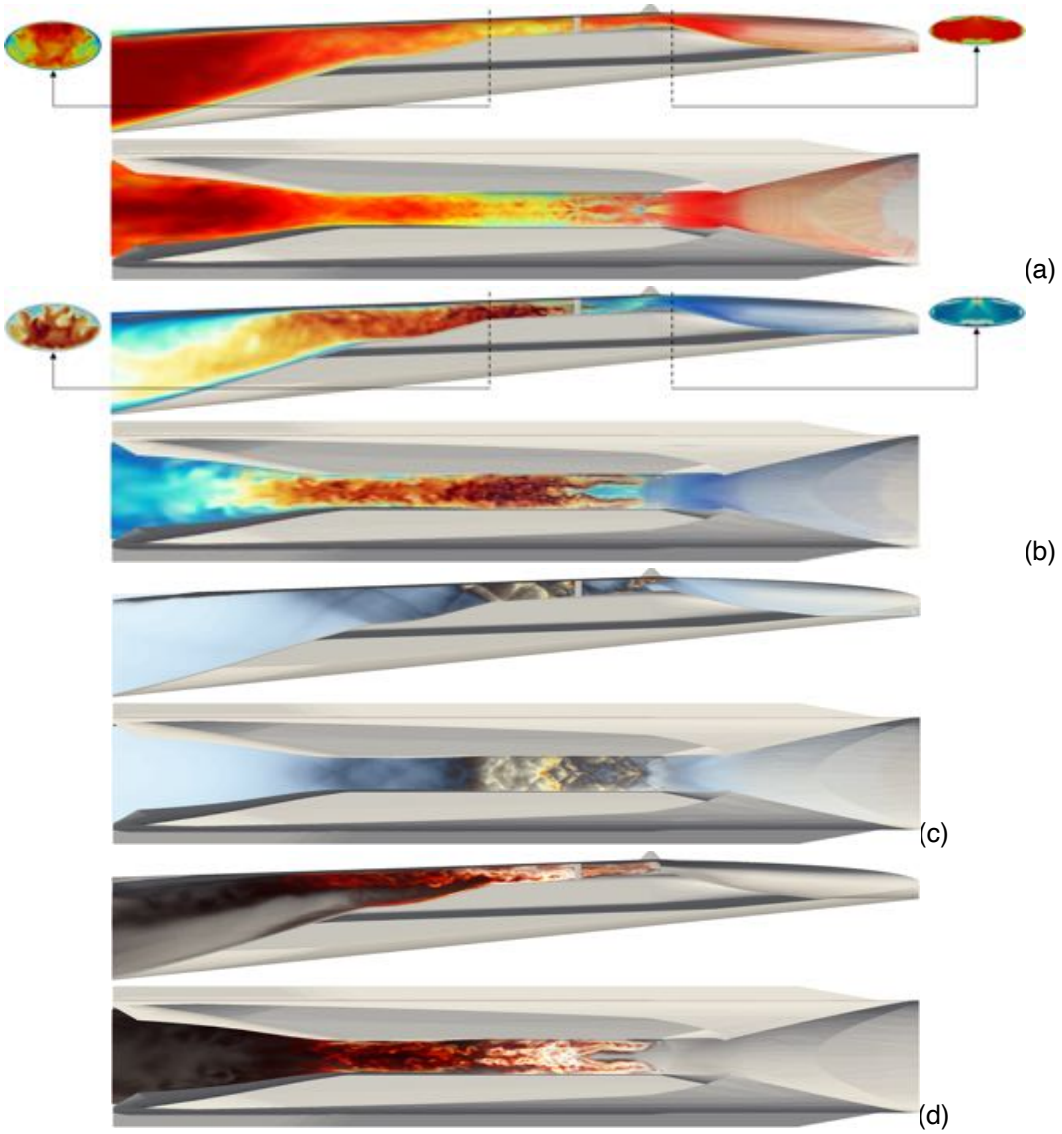

Fig. 14. Side- and top views from the combustion LES of the SSFE in terms of (a) axial velocity, vx, (b) temperature, T, (c), pressure, p, (d) and heat-release, Q, distributions. Two additional cross sections at the combustor intake (x=0.42 m) and at the end of the 1st combustor cross-sections (x=0.90 m) are also included at the right and left, respectively, to facilitate the understanding of the three-dimensional flow

Fig. 15 shows images from (a) experiments and (b) LES of the wall heat flux on the lower combustor wall (left panel) and on the intake surface (right panel), as well as (c) the wall pressure along the upper combustor surfaces as indicted. Regarding the wall heat flux the same colormaps are employed for the experimental and LES images on each section but different colormaps are used for the upper combustor wall and intake surface. The measured wall heat flux image for the intake surface are obtained from [22] whereas those of the lower combustor wall are provided by DLR as part of STRATOFLY. For the intake the wall surface heat flux increases downstream of the flat portion between the inlet lip and the downstream curved intake due to the compression of the flow. Imprints of the vortex pair close to the center plane and observed in Fig. 15-a and Fig. 15-b can be seen in both the experimental and computational images. For the lower combustor wall the deviations between the experimental and computational images are larger but the trends are similar with a region of high wall heat flux between the two semi struts and the full strut. Regarding the wall pressure, p, normalized by the free stream total pressure, p_t, in Fig. 15-c, results from both non-reacting and reacting cases are included together with the Rayleigh line as a reference. For the reacting case two peaks at x≈0.47 m and 0.65 m can be seen, these corresponds to the pressure increase due to injection at the semi-struts and full struts, respectively. The increase in p between x≈0.55 m and 0.9 m is due to the volumetric expansion caused by the exothermicity of combustion and is reasonably well reproduced by the LES. Both the experimental and computed peak pressures exceeds the maximum theoretical pressure rise due to H_2-air combustion indicated by the Rayleigh-line, suggests the presence of a strong shock-train throughout the combustor.

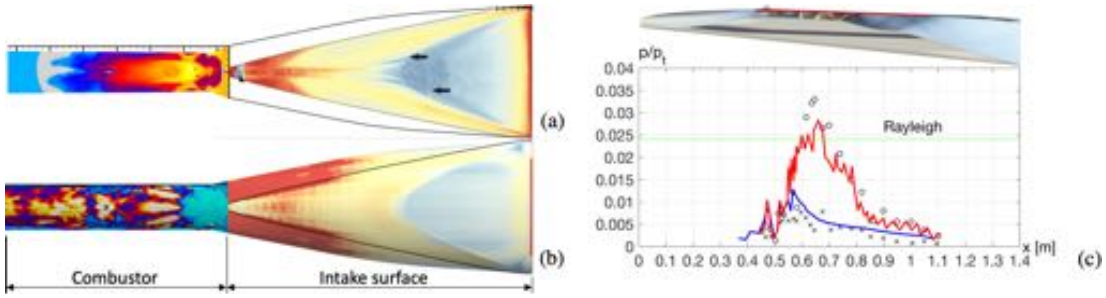

Fig. 15. Measured (a) and computed (b) wall heat flux on the lower combustor wall and on the intake. The same colormaps are used for the measured and computed images on each part but different colormaps are used for the lower combustor wall and intake. The experimental wall heat flux image for the intake is obtained from [x8] whereas those of the lower combustor wall are provided by DLR. In figure 15 experimental (symbols) and computed wall pressures, p, normalized by the free stream total pressure, pt, are presented for a non-reacting case (blue) and a reacting case (red) along the highlighted line

Fig. 16 compare cross sectional profiles of the time-averaged axial velocity, v_x, temperature, T, H_2 mass fraction, OH mass fraction and H_2O mass fraction at x=0.395, 0.550, 0.700, 0.800, 0.900 and 1.100 m along the combustor. Included are also line-of-sight experimental data from the DLR measurements. The highest velocities occur over the intake and the nozzle whereas lower velocities prevail in the combustor as a consequence of the complex flow pattern and the volumetric expansion due to the exothermicity. The flow accelerates along the 2nd combustor section and nozzle to produce thrust. The temperature is low over the intake and in the very first part of the combustor whereafter it increases. The imprints of the H_2 injection from the two semi-struts and the combustion occurring on the edges of the H_2 plumes from two semi-struts can easily be seen. The rapid spread of combustion across the entire combustor cross-section is also evident just downstream of the full-strut. The peak temperature occurs along the edges of the H_2 plumes and are just below the H_2-air temperature at stoichiometric conditions. Along the 2nd combustor section and nozzle the temperature decreases somewhat due to the expansion, whilst thrust is generated. Large amounts of H_2O are formed along the combustor as the H_2 is consumed. OH approximately represents the location of the combustion region and peak around the edges of the H_2 plumes and in the central part of the combustor downstream of the full strut as additional H_2 is injected here. Only very low values of OH are observed in the nozzle. Since NO_X exists in the freestream this will also enter the combustor and participate in the combustion reactions, and it appears than only small changes in Y_{NOX} prevail in the plume. The agreement between the LES predictions and the line-of-sight experimental data for Y_{H2O} and Y_{NO} is generally good, with the LES predictions revealing significant variations across the combustor as a

consequence of the complex, unsteady, vortex dominated, three-dimensional flow field.

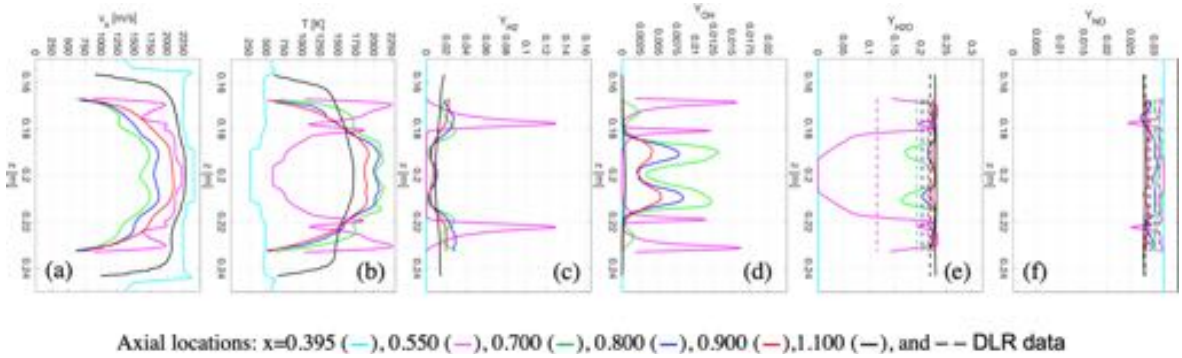

Fig. 16. Cross sectional profiles of the time-averaged (a) axial velocity, vx, (b) temperature, T, (c) H2 mass fraction, (d) OH mass fraction (e) H2O and (f) NOX mass fraction at six locations x=0.395, 0.550, 0.700, 0.800, 0.900 and 1.100 m along the combustor. Included is also line-of-sight experimental data from the DLR measurements

3.5 Noise analysis and noise reduction strategies

A laboratory scale nozzle was designed by VKI and manufactured by NLR for acoustic testing. The contours of the laboratory scale nozzle and the internal flow for a specific condition is shown in Fig. 17. This nozzle is able to capture key flow features which are believed to be possible noise mechanisms. A good agreement between wall pressures determined with CFD and experimental wall pressures is found. This makes it possible to couple flow topology information from the CFD solutions to noise predictions with semi-empirical jet noise models. An example CFD solution for this laboratory scale nozzle is shown in Fig. 18.

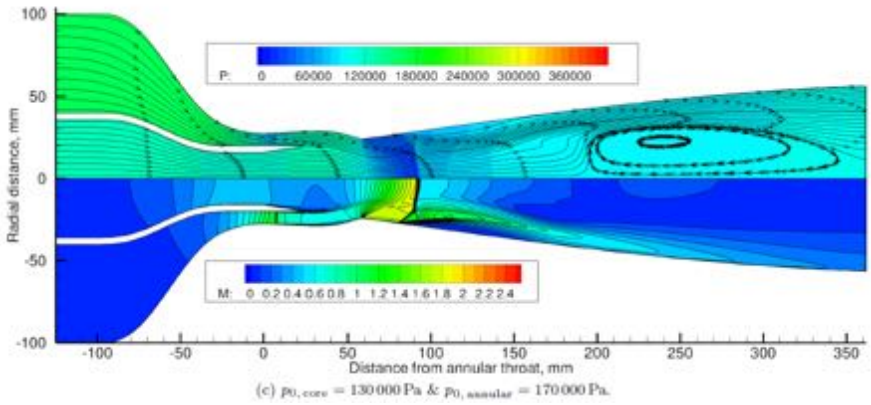

Fig. 17. CFD solution and contours of the laboratory scale nozzle for acoustic tests. This nozzle is able to capture key flow features which are believed to be possible noise mechanisms, here only one specific test condition is shown

Although CFD simulations show multiple possible sources of noise, the dominant source still seems to scale similar to jet noise in terms of sound power versus jet velocity. An interesting change in flow topology for the jet inside the STRATOFLY nozzle is observed. For outer jet Mach numbers > 0.6 (representing the ATR flow), the jet seems to re-attach inside the nozzle and an increase in high frequent noise is observed. Although this dual-mode behavior of the jet is interesting from scientific point of view, in terms of noise generation this is a secondary term. Therefore, the noise prediction is built upon the modelling of an equivalent jet inside the STRATOFLY nozzle by using Stone's semi-empirical jet noise model for inverted velocity profile jets [23].

Comparing noise measurements with semi-empirical jet noise predictions it can be concluded that aerodynamic effects of the STRATOFLY nozzle cannot be neglected. As first attempt to take the aerodynamic effect of the nozzle into account, the jet parameters which embody the input for Stone's semi-empirical jet noise model are retrieved from CFD calculations. Identifying the part of the internal nozzle flow solution that can be used to model an equivalent jet is to some extent susceptible to engineering judgement.

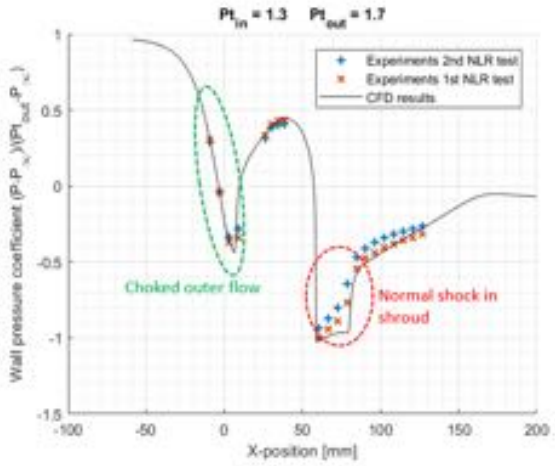

Fig. 18. Comparison between the experimental wall pressures and the wall pressure computed with CFD

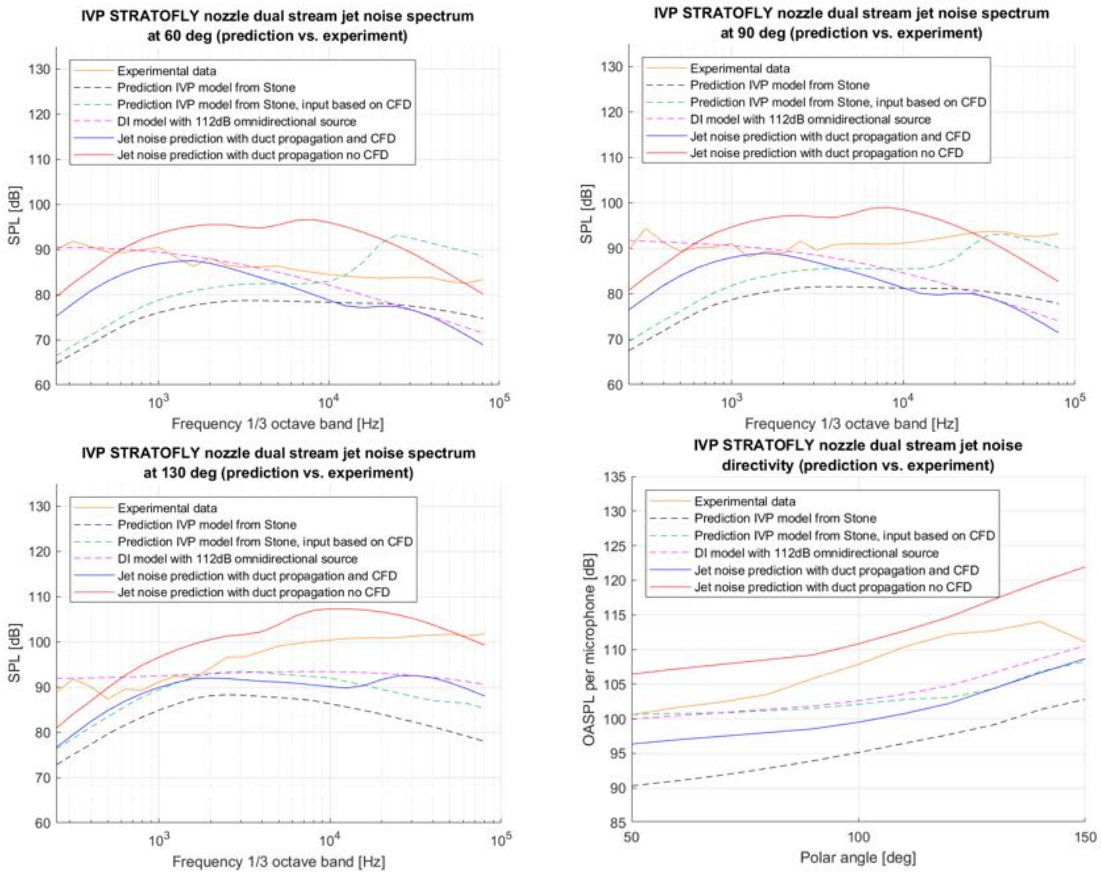

Fig. 19. Jet noise modelling approaches compared to measured spectra for different directivity angles. In clockwise direction starting at the top left figure: directivity angle of 60 degrees (0 degree is in flight direction), directivity angle of 90 degrees (lateral), directivity angle of 130 degrees, and the OASPL for all measured directivity angles

Besides the aerodynamic effect, the most dominant acoustic effect is that the STRATOFLY nozzle directs more acoustic energy towards downstream directivity angles. This effect becomes stronger with increasing frequency. The measured acoustic spectra and the calculated flow topologies with CFD show an analogy with a sound source in a duct radiating to free field conditions at the open end of the duct. Therefore, the noise from the STRATOFLY nozzle is in this research predicted by coupling Stone's semi-empirical jet noise model to a duct propagation model [24]. The jet noise model provides spectral information and sound power levels. But the typical jet noise directivity pattern is replaced by the duct propagation model. In this process the input for Stone's semi-empirical jet noise model can be either taken directly from CFD results or can be derived via isentropic flow relations in combination with some assumptions of the flow topology. For a noise impact study, the latter is more desirable since

CFD results are not required for each point along the flight path. The different noise modelling approaches which were attempted within the STRATOFLY project are shown for one test condition in Fig. 19.

Applying Stone's semi-empirical jet noise without taking the aerodynamic effect of the nozzle into account results in the black dashed line and underestimates the noise. When retrieving the input for Stone's model from CFD results in a supersonic outer jet (representing the ATR exhausts). The corresponding jet noise predictions are represented by the green dashed line. Although the OASPL are generally closer to measured levels, the directivity pattern is very different. The shock noise dominating the upstream directivity angles is not observed in the measurements. The pink dashed line represents the duct propagation model with an omnidirectional sound source and flat spectrum, illustrating the effect of the duct propagation model and a reasonable agreement is found. The subsequent solid blue and red line are predictions where Stone's semi-empirical jet noise model is coupled with this duct propagation model. The blue line uses input from CFD while the red line is obtained by making some assumptions about the flow topology.

The method that uses jet conditions from CFD directly results in a typical underprediction of 4 to 7dB in OASPL for each directivity angle, but can also be as large as 10dB. This accuracy is to some extent related to the engineering judgement that is involved when acquiring the input data from CFD. The method that derives the jet conditions via isentropic relations in combination with some assumptions of the flow topology is slightly more accurate and results in a typical overprediction of 3 to 6 dB in OASPL for each directivity angle. This overprediction is likely to be related to the neglection of losses and mixing in the annular stream tube. Therefore, it is believed that the overprediction will be smaller when aerodynamic losses are smaller at the region where the ATR jet interacts with the DMR flow. Overall, the agreement between the experimental and predicted SPL spectra is reasonable for this cold jet set-up.

A preliminary study has been performed to compute noise levels at certification points that can be compare to ICAO Annex 16. Note that only noise regulation for subsonic aircraft are available and no noise regulation is yet available for these type of aircraft. The jet noise during take-off is computed with the Stone's semi-empirical jet noise model in combination with the duct propagation model (red solid line of Fig. 19).The engine is modelled by VKI in EcoSimpro and the jet conditions at the nozzle exists (ATR and DMR) are used as input for Stone's semi-empirical jet noise model. The obtained results are shown in Table 1. Noise certification EPNdB levels for two configurations. A configuration without noise reduction and one with a mixer-ejecter and a perfect nozzle

. As can be seen these preliminary noise levels at certification points are very high when no noise reduction systems are in place. Therefore noise reduction systems are essential for this aircraft. The noise levels are dominated by jet mixing noise, which is mainly caused by the high speed internal jet originating from the ATR ducts. To reduce this jet mixing noise, the jet velocities should be reduced. To evaluate the effect of reducing this jet velocity, a first step is to let this ATR jet better mix with the flow from the DMR, resulting in a lower average jet velocity. To further reduce the average jet velocity external flow can be entrained in the combined nozzle, analogue to an ejector. Assuming the DMR, ATR and ejector flow mix perfectly and this combined flow expand and does not separate in the nozzle, much lower noise levels are found. The ratio of jet mass flow (ATR + DMR) over entrained air mass flow by the ejector is 0.07. The assumption of the perfectly expanded jet and no flow separation is very optimistic, but shows the potential of reducing the noise.

	Fly over	Sideline
Configuration without noise reduction	143.4	139.4
Optimal nozzle with mixer-ejector	63.1	61.9

Table 1. Noise certification EPNdB levels for two configurations. A configuration without noise reduction and one with a mixer-ejecter and a perfect nozzle

3.6 Trajectory optimization

The determination of operationally realistic flight mission characteristics, such as fuel consumption and flight time, requires the design of fuel-optimal flight trajectories where the vehicle's trip fuel converges to a minimum while simultaneously the amounts of pollutant emissions, like nitrogen oxide (NO) or

water vapor, emitted along the flight trajectory are reduced to a minimum. As these gaseous emissions have a different climate impact depending on the altitude and location (geodetic latitude (Lat) and longitude (Lon)) at which they are released, the climate-optimal mission profile might be lower (or higher) than the fuel-optimal flight profile of STRATOFLY-MR3. In order to investigate these trade-offs, trajectory calculations with various vertical profiles have been performed using a MATLAB-based mission simulator, the so-called Trajectory Calculation Module (TCM). This tool was originally developed by DLR's Institute of Air Transportation Systems [25] providing a fast-time, forward integration of aircraft state variables based on simplified point-mass equations of motion to calculate 4D flight trajectories. In the scope of STRATOFLY, TCM was adapted and extended with the aerodynamic, propulsive and emission databases of MR3 to meet the project requirements. Further information on this can be found in [26], [27], [28], [29] and [30].

Table 2 shows the simulation results for a parametric analysis of the initial cruise altitude (ICA) of MR3 starting from 95 000 ft to 120 000 ft with a vertical resolution of 1 000 ft. As reference mission, a flight route from Brussels (Lat: 50.843° | Lon: 1.263°) to Sydney (Lat: −35.896° | Lon: 150.146°) with a cruise Mach number of 8 and a maximum take-off weight (MTOW) of 400 t is considered resulting in a total travelled distance over ground of $18\,717.36\ km$ and a flight time of approximately $193\ \mathrm{min}$ ($3\mathrm{h}\ 13\ \mathrm{min}$). On the right-hand side of the table, the trip fuel calculation is based on a continuous climb cruise (CCC) modelling to keep the aerodynamic efficiency ($\mathrm{Lift/Drag}$) constant, while on the left-hand side, the ICA is kept constant during the cruise flight resulting in the same top of climb (TOC) and top of descend (TOD) within the horizontal flight profile.

ICA [ft]	Trip Fuel [kg]	NO [t]	H2O [t]	H2 [t]	Trip Fuel [kg]	NO [t]	H2O [t]	H2 [t]
120 000	165 176	7.5372	1 403.9	5.5863	165 478	7.5873	1 406.8	5.5535
119 000	164 887	7.5169	1 401.3	5.5868	165 227	7.5696	1 404.6	5.5532
118 000	164 576	7.4898	1 398.6	5.5869	164 947	7.5492	1 402.1	5.5537
117 000	164 261	7.4669	1 395.8	5.5873	164 667	7.5273	1 399.7	5.5543
116 000	163 946	7.4434	1 393.1	5.6057	164 342	7.5025	1 396.8	5.5546
115 000	163 636	7.4203	1 390.4	5.6067	164 023	7.4760	1 394.0	5.5547
114 000	163 487	7.4173	1 389.1	5.6070	163 659	7.4585	1 390.9	5.5550
113 000	163 409	7.4614	1 388.5	5.6072	163 135	7.4678	1 386.3	5.5554
112 000	158 994	8.5833	1 351.8	5.6139	162 205	7.5807	1 378.4	5.5568
111 000	159 613	8.6474	1 357.3	5.6137	160 833	7.8008	1 366.9	5.5583
110 000	160 118	8.7387	1 362.0	5.5608	160 249	8.0855	1 362.2	5.5602
109 000	161 407	8.8313	1 373.0	5.6108	160 087	8.4005	1 361.3	5.5606
108 000	162 797	8.9305	1 385.0	5.6462	160 341	8.6992	1 363.6	5.6125
107 000	163 873	9.0407	1 394.4	5.6448	161 166	8.8045	1 370.9	5.6117
106 000	165 003	9.1550	1 404.4	5.6441	162 157	8.9058	1 379.7	5.6113
105 000	166 205	9.2761	1 415.0	5.6438	163 170	9.0074	1 388.6	5.6102
104 000	167 478	9.4026	1 426.2	5.6430	164 267	9.1166	1 398.2	5.6083
103 000	168 799	9.5349	1 437.8	5.6415	165 383	9.2293	1 408.1	5.5890
102 000	170 181	9.6722	1 450.0	5.6394	166 494	9.3387	1 417.9	5.5882
101 000	171 619	9.8128	1 462.6	5.6389	167 823	9.4681	1 429.6	5.5869
100 000	173 120	9.9575	1 475.8	5.6378	169 003	9.5804	1 440.0	5.5858
99 000	174 708	10.1099	1 489.8	5.6366	170 809	9.7151	1 455.5	5.6401
98 000	176 710	10.2929	1 507.4	5.6307	172 049	9.8326	1 466.5	5.6390
97 000	170 341	9.3633	1 452.8	5.6372	172 314	9.7966	1 469.1	5.6385
96 000	172 648	9.5772	1 473.2	5.6360	172 411	9.7379	1 470.2	5.6373
95 000	175 361	9.8275	1 497.1	5.6337	172 559	9.6888	1 471.8	5.6375

Table 2. Parametric analysis of initial cruise altitude of MR3 for a flight route from BRU to SYD with cruise Mach 8 and MTOW 400 t

For an altitude range segment between 95 000 ft and 109 000 ft it can be seen, that the CCC is superior to the constant cruise altitude approach in terms of minimum fuel consumption for MR3. For altitudes beyond 109 000 ft, the CCC lacks of performance resulting in a slightly higher fuel consumption compared to the constant altitude cruise flight program. For the latter, an ICA of 112 000 ft results in a fuel-optimal trajectory with $158\,994\ t$ of trip fuel, whereas for the CCC, an ICA of 109 000 ft ensures a fuel-optimal trajectory with $160\,087\ t$ of trip fuel. Since water vapor emissions are directly correlated to the vehicle's total amount of burned hydrogen (H_2), these statements also hold for a minimum-emissions trajectory in terms of water vapor where $1\,351.8\ t$ of H_2O ensures a minimum-emissions trajectory for the constant altitude cruise flight program and $1\,361.3\ t$ of H_2O guarantees a minimum-emissions trajectory for the CCC operation. For the total amount of NO, an ICA of 114 000 ft ensures a minimum-emissions trajectory resulting in $7.4173\ t$ of NO for a constant altitude cruise flight program and $7.4585\ t$ of NO for the CCC flight program.

Summarizing the statements from above a trade-off between a fuel- and H_2O-optimal trajectory and a NO-optimal trajectory can be identified for an ICA of 109 000 ft, 112 000 ft and 114 000 ft. To find an

adequate compromise between these ICAs, we assume that the major impact from supersonic and hypersonic aviation on climate is caused by water vapor ([31], [32]). Furthermore, as per [7], the climate impact of water vapor emissions is higher at higher altitudes (in the current state of this study, a preliminary prediction for the climate impact can only be made by the total amount of emitted emissions along the aircraft's flight trajectory). Thus, choosing an ICA of 109 000 ft with the CCC flight program seems to provide the best solution for this trade-off investigation. Although the NO emissions are approximately 11 % higher compared to an ICA of 114 000 ft, the trajectory design satisfies a fuel-optimal flight profile with a minimum amount of water vapor emissions being emitted in the lowest ICA possible. Fig. 20 shows the final result of the optimal trajectory design for MR3 including the altitude and Mach profile plotted over the flight time.

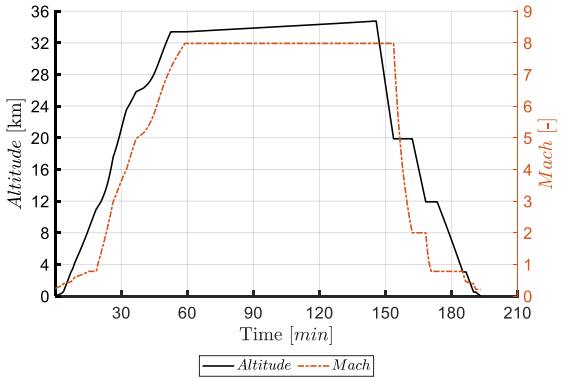

Fig. 20: Optimal altitude and Mach profile over time for MR3 with an initial cruise altitude of 109 000 ft

3.7 Impact on atmospheric composition and climate

The climate impact of hypersonic transport is a key question in the development of high speed transportation. Both, the aircraft design and the trajectory (route and flight altitude), are important factors which determine the impact on climate. Especially the cruise altitude is important. A preliminary assessment of the impact of hypersonic flights on atmospheric composition and climate has been performed based on two base case scenarios: one for the ZEHST and one for the LAPCAT (PREPHA version) vehicles analyzed in the framework of the HIKARI European project. All scenarios have the same total transport volume, however, the market penetration of the ZEHST and LAPCAT(PREPHA) technology differs: 9.8% and 26%, respectively. The total emissions of pollutants for these two scenarios amount at 16.7 Mt H_2O and 40 kt NO_2 for ZHEST and 26.5 Mt H_2O and 61 kt NO_2 for LAPCAT (PREPHA).

The well-established LMDZ-INCA and EMAC global chemistry-climate models were applied to investigate the impact of the ZHEST and LAPCAT (PREPHA) fleet on atmospheric composition. Quasi-steady state results from either model for the change in the water vapor and ozone mixing ratios are shown in Fig. 21 for LMDZ-INCA and in Fig. 22 for EMAC. The results clearly exhibit a similar response pattern for either model. An increase is found around the main cruise altitude (26 km in the case of ZHEST and 35 km in the case of LAPCAT (PREPHA) in northern hemisphere. The maximum impact on the water vapor distribution arises from the LAPCAT scenario with a maximum increase reaching 25% at the 35km flight altitude (12% for the ZHEST scenario). In the case of ozone, the NO_x emitted by the aircraft but also the hydrogen radicals (HO_x) arising from the enhanced water vapour concentrations are responsible for a destruction reaching 3% in the case of LAPCAT and less than 1% in the case of ZEHST.

The climate impact of hypersonic emissions at stratospheric altitudes is dominated by the increase in water vapor concentration and the in turn increased radiative forcing. Fig. 21 and Fig. 22 clearly show a larger increase of water vapor and larger decrease for ozone for the LAPCAT (Prepha) aircraft due the higher cruise altitude and as a result a longer residence time of hypersonic emissions. A conceptual comparison of different aircraft designs and the related residence time is presented in **Figure 3**. The radiative forcing related to the increase in stratospheric water vapor will be presented in another separate publication. Nonetheless, a positive correlation of additional water vapor and an increase in radiative forcing is clearly visible. However, even though the LAPCAT (Prepha) aircraft creates a larger perturbation of water vapor, the design is preferable over ZEHST in terms of climate impact due to the

larger passenger capacity and thus lower climate impact in terms of temperature change per revenue passenger kilometers.

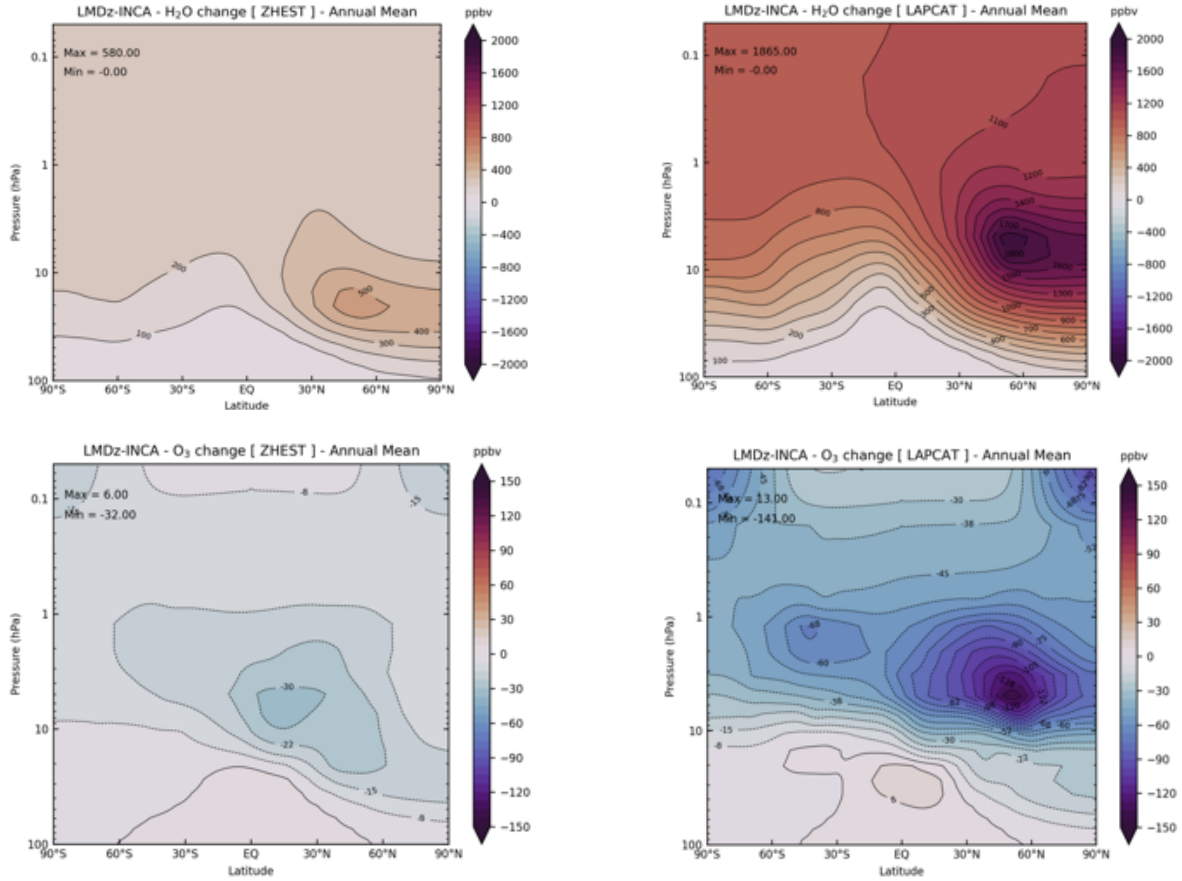

Fig. 21. Zonal mean distributions of the atmospheric water vapor and ozone mixing ratio changes (ppbv) calculated by the LMDZ-INCA model and due to a fleet of hypersonic aircraft: ZHEST (left), LAPCAT (right)

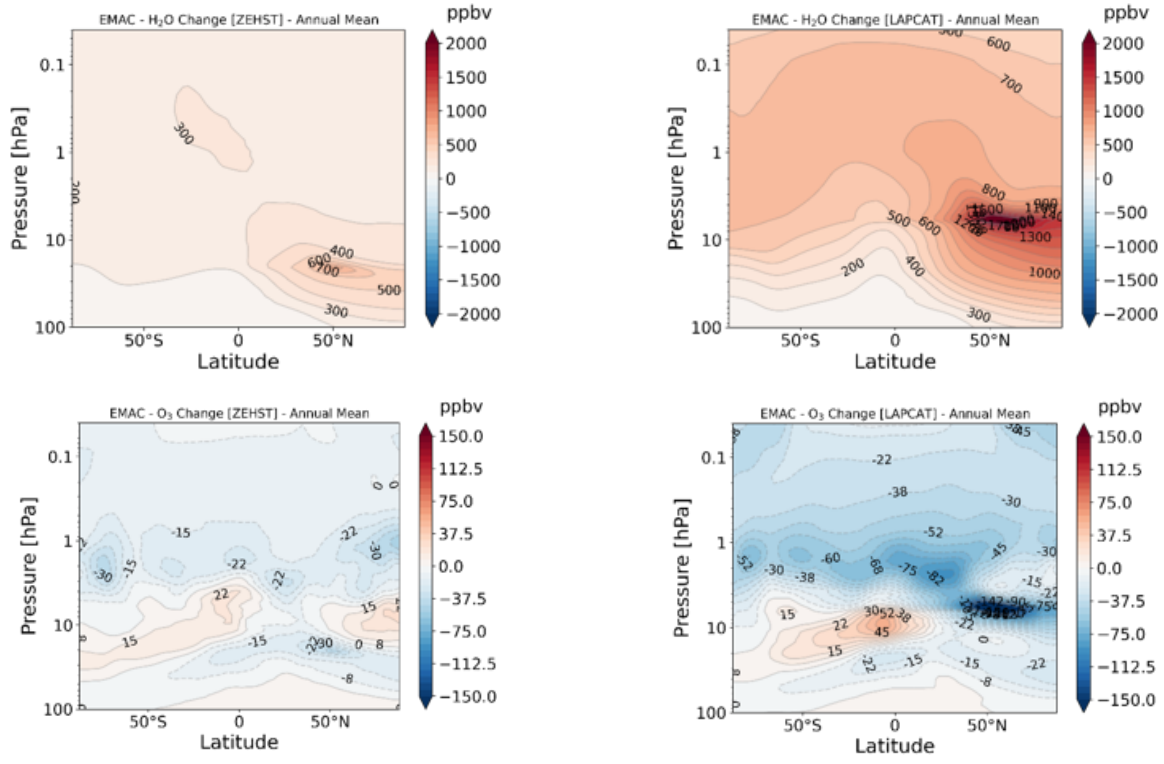

Fig. 22. Zonal mean distributions of the atmospheric water vapor and ozone mixing ratio changes (ppbv) calculated by the EMAC model and due to a fleet of hypersonic aircraft: ZHEST (left), LAPCAT (right)

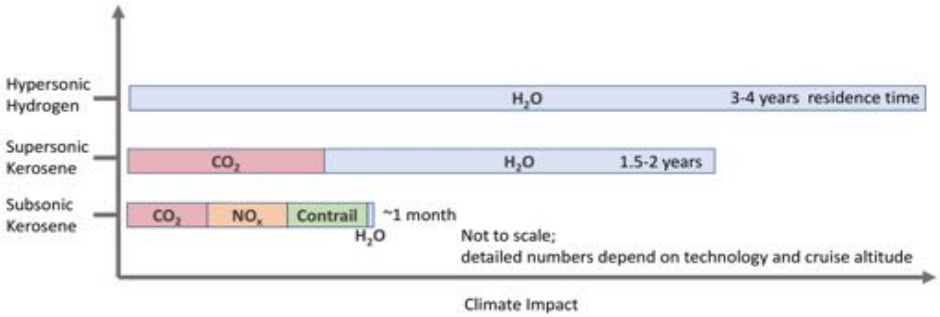

Fig. 23. Residence time of water vapor perturbation for different aircraft designs (hypersonic fueled with hydrogen, supersonic and subsonic fueled with kerosene). This representation is not to scale. Values of hypersonic vehicles are based on ZEHST and LAPCAT emissions [33]

4. CONCLUSIONS

The STRATOFLY MR3 vehicle' and mission concept current evolution is described in this paper, presenting the main results achieved so far to solve the main issues related to thermal and structural integrity, low-emissions combined propulsion cycles, subsystems design and integration, including all the attempts to reduce the climate, environmental and noise impact.

5. ACKNOWLEDGMENTS

The H2020 STRATOFLY Project has received funding from the European Union's Horizon 2020 research and innovation programme under Grant Agreement No. 769246.

6. References

[1] T. Langener, S. Erb, J.Steelant, TRAJECTORY SIMULATION AND OPTIMIZATION OF THE LAPCAT-MR2 HYPERSONIC CRUISER CONCEPT, Proceedings of the 29th Congress of the International Council of the Aeronautical Sciences, St. Petersburg, Russia, September 2014.

[2] Steelant, Johan. ATLLAS: Aero-thermal loaded material investigations for high-speed vehicles", 15th AIAA International Space Planes and Hypersonic Systems and Technologies Conference. 2008.

[3] Steelant, J., Varvill, R., Defoort, S., Hannemann, K., Marini, M.: Achievements Obtained for Sustained Hypersonic Flight within the LAPCAT-II Project, 20th AIAA International Space Planes and Hypersonic Systems and Technologies Conference, Glasgow, Scotland, AIAA- 2015-3677, 2015.

[4] E. Blanvillain, E. Gallic, "HIKARI: Paving the way towards high speed air transport", 20th AIAA International Space Planes and Hypersonic and Technologies Conference. Glasgow, Scotland, 2015.

[5] J. Steelant et al., "Conceptual Design of the High-Speed Propelled Experimental Flight Test Vehicle HEXAFLY", 20th AIAA International Space Planes and Hypersonic Systems and Technologies Conference, Glasgow, Scotland, 2015.

[6] N. Favaloro et al. "Design analysis of the high-speed experimental flight test vehicle HEXAFLY International", 20th AIAA International Space Planes and Hypersonic Systems and Technologies Conference, Glasgow, Scotland, 2015.

[7] Viola, N.; Fusaro, R.; Gori, O.; Marini, M.; Roncioni, P.; Saccone, G.; Saracoglu, B.; Ispir, A.C.; Fureby, C.; Nilson, T.; et al. STRATOFLY MR3–how to reduce the environmental impact of high-speed transportation. In Proceedings of the AIAA Scitech 2021 Forum, 11 January 2021; p. 1877; doi:10.2514/6.2021-1877.

[8] Ferretto, D.; Fusaro, R.; Viola, N. Innovative Multiple Matching Charts approach to support the conceptual design of hypersonic vehicles. *Proc. Inst. Mech. Eng. Part G J. Aerosp. Eng.* **2020**, *234*, 1893–1912, doi:10.1177/0954410020920037.

[9] Ferretto, D.; Fusaro, R.; Viola, N. A conceptual design tool to support high-speed vehicle design. In Proceedings of the AIAA AVIATION 2020 FORUM, 15–19 June 2020 Virtual Event; p. 2647, doi:10.2514/6.2020-2647.

[10] Langener, T.; Erb, S.; Steelant, J. Trajectory Simulation and Optimization of the LAPCAT MR2 Hypersonic Cruiser Concept. In Proceedings of the 29th Congress of the International Council of the Aeronautical Sciences, St. Petersburg, Russia, 7–12 September 2014; ICAS 2014 428.

[11] Viola,N.;Roncioni,P.;Gori, O.; Fusaro, R. Aerodynamic Characterization of Hypersonic Transportation Systems and Its Impact on Mission Analysis. *Energies* **2021**,*14*,3580. https://doi.org/10.3390/en14123580

[12] Rodriguez-Segade, M.; Hernandez, S.; Diaz, J.; Baldomir, A.; Lopez, D. Structural Scheme for the Propulsion Systems and the Complete Hypersonic STRATOFLY Vehicle. In AIAA SciTech 2020 Forum; American Institute of Aeronautics and Astronautics: Orlando, FL, 2020. https://doi.org/10.2514/6.2020-1107.

[13] Rodriguez-Segade Alonso, M.; Hernandez, S.; Diaz, J.; Baldomir, A. A Bi-Level Approach for the Structural Optimization of the Hypersonic STRATOFLY MR3 Vehicle. In AIAA SciTech 2021 Forum; American Institute of Aeronautics and Astronautics: VIRTUAL EVENT, 2021. https://doi.org/10.2514/6.2021-0098.

[14] Goncalves, P. M., Ispir, A. C., & Saracoglu, B. H. (2019). Development and optimization of a hypersonic civil aircraft propulsion plant with regenerator system. In AIAA Propulsion and Energy 2019 Forum (p. 4421).

[15] [Menon S. & Fureby C.; 2010, "Computational Combustion", In Encyclopedia of Aerospace Engineering, Eds. Blockley R. & Shyy W., John Wiley & Sons.

[16] Yoshizawa A., Kobayashi K., Kobayashi T. & Taniguchi N.; 2000, "A Nonequilibrium Fixed-Parameter SubGrid-Scale Model Obeying the Near-Wall Asymptotic Constraint", Phys. Fluids, 12, p 2338.

[17] Sabelnikov V. & Fureby C.; 2013, "LES Combustion Modeling for High Re Flames using a Multi-phase Analogy", Comb. Flame, **160**, p 83.

[18] Zettervall N. & Fureby C.; 2018, "A Computational Study of Ramjet, Scramjet and Dual-mode Ramjet Combustion in Combustor with a Cavity Flameholder", AIAA 2018-1146.

[19] Fureby C.; 2020, "Subgrid Models, Reaction Mechanisms and Combustion Models in LES of Supersonic Combustion", AIAA.J., **59**, p 215.

[20] Nilsson T. Zhong S. & Fureby C.; 2021, "Hydrogen Jet Combustion in High Enthalpy Supersonic Crossflow", Phys. Fluids, **33**, 035133.

[21] Celik I., Cehreli Z.N. & Yavuz I.; 2005, "Index of Resolution Quality for Large Eddy Simulations", J. Fluids Eng., 127, p 949.

[22] Martinez Schramm J., Karl S., Hannemann K. & Ozawa H.; 2018, "Ultra-fast Temperature Sensitive Paint Shock Tunnel Heat Flux Measurements on the Intake of the LAPCAT II Small Scale Flight Experiment Configuration", HiSST: Int. Conf. on High-Speed Vehicle Science Technology, 26-29 November, Moscow, Russia.

[23] Stone, J., Zola, C., & Clark, B. (1999). An improved model for conventional and inverted-velocity-profile coannular jet noise. In *37th Aerospace Sciences Meeting and Exhibit* (p. 78).

[24] Day, A., Hansen, C., & Bennett, B. (2009). Duct directivity index applications. *Acoustics Australia*, *37*(3-93).

[25] Linke, F.: Environmental Analysis of Operational Air Transportation Concepts. PhD thesis, Technical University of Hamburg (2016)

[26] Bodmer, D.: Trade-Offs and Trajectory Optimization – Interim Report, GA-769246 STRATOFLY, Technical University of Hamburg (2020)

[27] Scigliano, R., Marini, M., Roncioni, P., Fusaro, R., Viola, N.: STRATOFLY High-Speed Propelled Vehicle Preliminary Aero-Thermal Design. In: International Conference on Flight Vehicles, Aerothermodynamics and Re-entry Missions and Engineering, pp. XX–XX. Monopoli, Italy (2019)

[28] Nista, L., Saracoglu, B.H.: Numerical investigation of the STRATOFLY MR3 propulsive nozzle during supersonic to hypersonic transition. In: AIAA Propulsion and Energy 2019 Forum, pp. 1–16. Indianapolis, Indiana, USA (2019). https://doi.org/10.2514/6.2019-3843

[29] Ispir, A.C., Saracoglu, B.H.: Development of a 1D dual mode scramjet model for a hypersonic civil aircraft. In: AIAA Propulsion and Energy 2019 Forum, pp. 1–9. Indianapolis, Indiana, USA (2019). https://doi.org/10.2514/6.2019-3842

[30] Goncalves P.M., Ispir A.C., Saracoglu B.H., Development and optimization of a hypersonic civil aircraft propulsion plant with regenerator system. In: AIAA Propulsion and Energy 2019 Forum, pp. 1–10. Indianapolis, Indiana, USA (2019). https://doi.org/10.2514/6.2019-4421

[31] IPCC: Special report on aviation and the global atmosphere, edited by: Penner, J. E., Lister, D. H., Griggs, D. J., Dokken, D. J., and McFarland, M., Intergovernmental Panel on Climate Change, Cambridge University Press, New York, NY, USA (1999)

[32] Grewe, V., Stenke, A., Ponater, M., Sausen, R., Pitari, G., Iachetti, D., Rogers, H., Dessens, O., Pyle, J., Isaksen, I.S.A., Gulstad, L., Søvde, O.A., Marizy, C., Pascuillo, E.: Climate impact of supersonic air traffic: An approach to optimize a potential future supersonic fleet - Results from the EU-project SCENIC. Atmosphere Chemistry and Physics. no. 7., pp. 5129-5145 (2007). 10.5194/acpd-7-6143-2007.

[33] Grewe, V., Climate Impact Hypersonic Aviation. von Karman Institute Lecture Series, 25.-27. May 2021, Lecture Series.